

Cite this: *Sustainable Energy Fuels*, 2025, 9, 1797

## Efficiency boost in perovskite solar cells *via* $\text{TiO}_2$ nanodiscs embedded in the $\text{MoSe}_2$ electron transport layer revealed by optoelectronic simulations<sup>†</sup>

Javad Maleki, <sup>‡a</sup> Maryam Shahrostami, <sup>‡a</sup> Siming Huang<sup>b</sup> and Mojtaba Abdijalebi <sup>\*b</sup>

To improve the performance of inverted perovskite solar cells (IPSCs), we introduce a novel approach to enhance the devices' efficiency notably using the Finite Element Method (FEM). Our novel strategy incorporates a cutting-edge metasurface-based reflector featuring titanium dioxide ( $\text{TiO}_2$ ) nanodiscs within a  $\text{MoSe}_2$  layer, employed as an electron transport layer (ETL). Demonstrating a substantial improvement in light reflection from the lower part of the structure, the  $\text{TiO}_2$  nanodiscs as a metasurface-based reflector enhance electron transfer. Notably, the metasurface-based perfect reflector, incorporating  $\text{TiO}_2$  nanodiscs, outperforms other  $\text{TiO}_2$  nanocube variations with an impressive light reflectance of 97.95%. Exploring different materials for ETLs and hole transfer layers (HTLs), we identify molybdenum diselenide ( $\text{MoSe}_2$ ) as a potent secondary absorbent material, featuring a smaller bandgap than the primary absorbent  $\text{CH}_3\text{NH}_3\text{PbI}_3$  (MAPbI<sub>3</sub>), thereby intensifying the electric field within the active layer and improving Power Conversion Efficiency (PCE). In the final evaluation, our inverted metasurface-based device structure (indium tin oxide (ITO)/cuprous oxide ( $\text{Cu}_2\text{O}$ )/MAPbI<sub>3</sub>/ $\text{TiO}_2$  nanodiscs and  $\text{MoSe}_2$ /aluminum (Al)/silicon dioxide ( $\text{SiO}_2$ )) significantly enhances the solar cell's electrical characteristics compared to the planar reference structure (ITO/copper(I) thiocyanate ( $\text{CuSCN}$ )/MAPbI<sub>3</sub>/ $\text{TiO}_2$ /Al), with noteworthy increases in short circuit current density ( $J_{sc}$ ), open circuit voltage ( $V_{oc}$ ), and PCE values from 17.98 mA cm<sup>-2</sup> to 21.91 mA cm<sup>-2</sup>, 1.03 V to 1.07 V, and 15.33% to 19.17%, respectively. This comprehensive investigation underscores the promising potential of our proposed inverted metasurface-based device structure for advancing solar cell technology.

Received 11th October 2024  
Accepted 17th February 2025

DOI: 10.1039/d4se01414f  
[rsc.li/sustainable-energy](http://rsc.li/sustainable-energy)

## 1. Introduction

The increasing demand for clean energy has become a critical issue due to the shortage of fossil fuel resources, the resulting air pollution, and the urgent need for immediate action to combat climate change.<sup>1–3</sup> Therefore, the rapid development of new energy harvesting technologies to provide alternative clean, renewable, and sustainable energy from natural sources, such as solar—the most abundant energy resource—is crucial.<sup>4–7</sup> In recent years, perovskite solar cells have achieved significant advancements, including higher PCE and lower manufacturing costs compared to the market-dominant silicon solar cells.<sup>8–11</sup> Perovskite materials find application in diverse single-junction

and tandem solar cell architectures, both for indoor and outdoor environments.<sup>12–16</sup> Among all different subgroups of perovskites, there has been extensive interest on metal halide perovskite solar cells. This is widely because of their remarkable optical and electrical properties such as noticeably high light absorption spectrum, simple fabrication processes, and substantial carrier mobility and diffusion lengths.<sup>17,18</sup> The selection of MAPbI<sub>3</sub> is driven by the abundance of research literature and datasets, enabling a data-driven approach to model building.<sup>19–22</sup> Therefore, MAPbI<sub>3</sub> was used as the perovskite active layer in this work due to the wide light absorption spectra (wavelengths region including 300 to 800 nm) and proper carrier transfer (high carrier mobility and permittivity).<sup>23–25</sup> In order to enhance the solar cell's PCE, metasurface structures were developed to manipulate the incoming incident light.<sup>26–28</sup> Furthermore, metasurface structures are easy to fabricate and have proven to increase the light absorption because of the internal light reflections that cause light interactions with other layers.<sup>29,30</sup> Thus, deploying this technology in solar cell devices has raised attention and is currently used by

<sup>a</sup>Department of Electrical and Computer Engineering, Tarbiat Modares University (TMU), Tehran, Iran

<sup>b</sup>Institute for Materials Discovery, University College London, Malet Place, London, WC1E 7JE, UK. E-mail: [m.jalebi@ucl.ac.uk](mailto:m.jalebi@ucl.ac.uk)

† Electronic supplementary information (ESI) available. See DOI: <https://doi.org/10.1039/d4se01414f>

‡ These authors contributed equally to this work.



many researchers.<sup>31–34</sup> The integrated periodic nanostructured metasurfaces perform mainly through the Snell's law by trapping the incident light and inclining the total absorption of the solar cell.<sup>35,36</sup> Therefore, opting the material, shape and size of the nanostructure have serious consequence in the system's efficiency.<sup>37–40</sup> The TiO<sub>2</sub> nanodiscs can be grown on an Al substrate using a hydrothermal technique involving several steps.<sup>41,42</sup> A research on a nanostructured cubic metasurface reflector consisting of three layers of TiO<sub>2</sub>/Ag/SiO<sub>2</sub> proved to have a promising performance.<sup>43</sup> Therefore, in this paper, different shapes (nanodiscs and three various types of nanocubes) of TiO<sub>2</sub> were selected as the integrated metasurface nanostructure and the ETL on top of a planar Al/SiO<sub>2</sub> structure to reach the optimized structure. Then, the nanostructure's size and position's degrees were optimized for one of the nanocubic structures to reach the highest light reflection to increase the total light absorption of the solar cell. However, the light reflection was further improved by using TiO<sub>2</sub> nanodiscs instead. In order to increase the light reflection by the metasurface nanostructure, another optical study was done on discovering the material with suitable refractive index to surround the TiO<sub>2</sub> nanostructure. Thereby, ETL materials such as zinc oxide (ZnO), Al-doped zinc oxide (AZO), cerium oxide (CeO<sub>2</sub>), and titanium dioxide-graphene (5%) (TiO<sub>2</sub>-Graphen (5%) or TiGO-5) were studied. Plus, this is a well-recognized issue that TiO<sub>2</sub> only absorbs the visible light with the wavelength range of 300 to almost 400 nm.<sup>44</sup> With regard to this, it can be argued that an inverted solar cell would be more beneficial to increase the total light reflection inside the device since the TiO<sub>2</sub> nanostructure would be placed on a non-transparent contact like Al, which results in more light interaction in the ETL and consequently other layers. The IPSCs have become prominent in light of their advantageous characteristics like high stability and PCE.<sup>45,46</sup> They consist of a reversed architecture, where the ETL and HTL are replaced by each other.<sup>47</sup> Hence, the HTL material was required to have a low light absorption rate in order for the incident light to reach the active layer and the ETL as well. For this reason, different materials including CuSCN, Spiro-OMeTAD, copper(I) iodide (CuI), and CuO<sub>2</sub> were studied as HTL. Additionally, another active layer, MoSe<sub>2</sub>, was used to enhance the light absorption, which was located below the MAPbI<sub>3</sub> layer. MoSe<sub>2</sub> exhibits a compelling set of properties that make it a promising candidate for integration into perovskite solar cells.<sup>48</sup> Notably, its high electron mobility facilitates efficient charge transport, minimizing energy losses and boosting overall efficiency.<sup>49,50</sup> Furthermore, MoSe<sub>2</sub> offers tunable electrical characteristics, allowing for precise energy level alignment within the perovskite layer, crucial for optimal charge transfer.<sup>51</sup> Its strong light absorption across the visible and near-infrared spectrum maximizes the utilization of solar energy, while its robust chemical and thermal stability ensure long-term device performance and reliability under diverse operating conditions.<sup>52</sup> Finally, the layered structure of MoSe<sub>2</sub> aligns well with the architecture of perovskite solar cells, potentially simplifying integration and enabling facile exfoliation for device fabrication.<sup>53</sup> Finally, the results were compared to reach the optimized device with the highest PCE,

resulted in the improvement in values of  $J_{sc}$ ,  $V_{oc}$ , and PCE from 17.98 mA cm<sup>-2</sup> to 21.91 mA cm<sup>-2</sup>, 1.03 V to 1.07 V, and 15.33% to 19.17%, respectively.

## 2. Theory

In this section, the electrical and optical models and their coupling were discussed. Additionally, the simulation details related to these models were also described.

### 2.1. Optoelectronic model

Two different sets of optical and electrical equations were analyzed in order to calculate various parameters, as shown in Fig. 1. The optical equations utilized Maxwell's equation (eqn (1)) to determine the electric field ( $E$ ) with the input parameters including: refractive index ( $n$ ) and extinction coefficient ( $k$ ) of all layers.

$$\nabla \times (\nabla \times E) - k_0 \epsilon_r E = 0 \quad (1)$$

The calculation of the electric field resulted in the optical outputs such as reflection, absorption, and the optical generation rate for electrons and holes ( $G_n$ ,  $G_p$ ). The optical generation rate referred to the number of the generated electron–hole pairs at each point in the device due to the absorption of photons.

The dark current density and electron–hole distribution and recombination rate of electron and hole ( $R_n$ ,  $R_p$ ) was then calculated by solving the Poisson's and Continuity equations (eqn (2)–(4)), as well as the related equations to Shockley–Reed–Hall (SRH) recombination by applying the input parameters such as band gap ( $E_g$ ), electron affinity ( $\chi$ ), dielectric constant ( $\epsilon$ ), electron mobility ( $\mu_n$ ), hole mobility ( $\mu_p$ ), density state of valence band ( $N_V$ ), density state of conduction band ( $N_C$ ), acceptor and donor doping ( $N_A, N_D$ ), electron lifetime ( $\tau_n$ ), and hole lifetime ( $\tau_p$ ) of each layer.

$$\nabla \cdot (\epsilon_0 \cdot \epsilon_r \cdot \nabla \varphi) = -\rho \quad (2)$$

$$\frac{\partial n}{\partial t} = \frac{1}{q} \nabla J_n + G_n - R_n \quad (3)$$

$$\frac{\partial p}{\partial t} = \frac{1}{q} \nabla J_p + G_p - R_p \quad (4)$$

The current density in the cell was solved by coupling the two sets of equations. Fig. 1 illustrates the flowchart of the optoelectronic model. A standard AM 1.5 with the light intensity of 100 mW cm<sup>-2</sup> perpendicular to the surface was used as the incoming light source. Different layers behaved differently after interacting with the incoming electric field according to their  $n$  and  $k$ . The dark current density, which has a direct relation with the amount of SRH recombination in the system, is calculated by solving the electric model without considering the incident electric field. To calculate the  $J_{sc}$ , both optical and electrical physics were solved, simultaneously. In this study, the



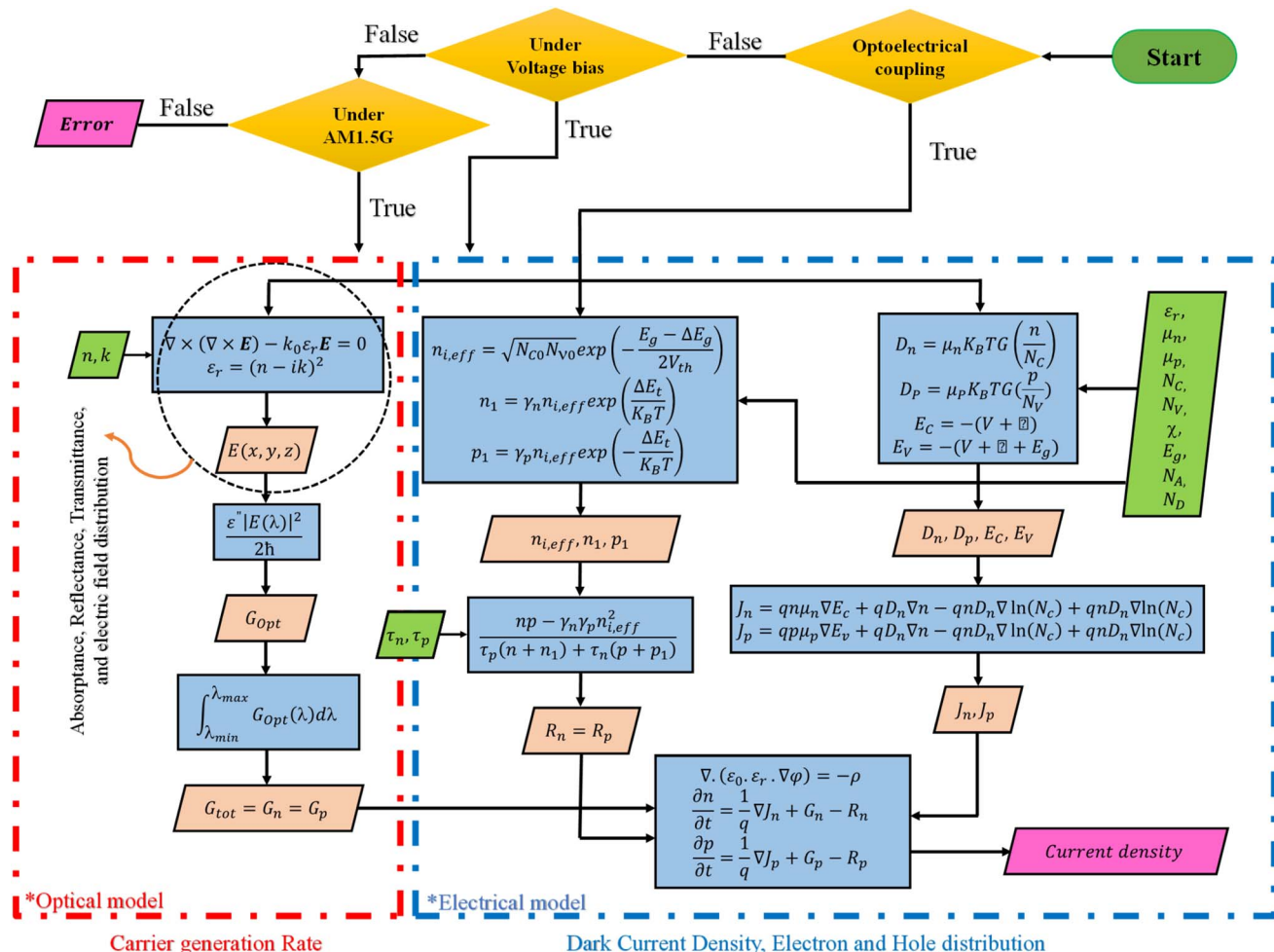


**Fig. 1** Flowchart of the optoelectronic model to calculate solar cell parameters, where the red and blue sections are considered as separated optical and electrical models, respectively. In the optical model, the Maxwell's equation is solved to reach the carrier generation rate, whereas in the electrical model, the Poisson's and Continuity equations are solved to achieve the dark current density. The coupling of two models results in the photocurrent density of the solar cell.

wavelength in the range of 300 to 1200 nm was swept with 20 nm steps, and the current density spectrum was calculated in terms of wavelength. A sum of current densities in the

abovementioned wavelength range with 20 nm steps was added to the dark current density to calculate the total current density in terms of voltage. In addition to SRH recombination for the

**Table 1** Electrical parameters for the used materials in the electrical model, where  $\epsilon_r$  denotes the dielectric constant,  $N_C$  and  $N_V$  present the density states of conduction and valence bands, respectively,  $\mu_n$  and  $\mu_p$  show the electron and hole mobility, respectively,  $\chi$  is the electron affinity,  $E_g$  is the band gap,  $N_A$  and  $N_D$  are the acceptor and donor doping, respectively, and  $\tau_n$  and  $\tau_p$  show the electron and hole lifetime, respectively

Parameters	ZnO	AZO	CeO <sub>2</sub>	TiGO-5	CuSCN	Spiro-OMeTAD	CuI	Cu <sub>2</sub> O	MAPbI <sub>3</sub>	TiO <sub>2</sub>	MoSe <sub>2</sub>
$\epsilon_r$	9	9	9	7.3	10	3	12.5	7.5	6.5	9	7.29
$N_C$ (cm <sup>-3</sup> )	$2.2 \times 10^{18}$	$2.2 \times 10^{18}$	$1 \times 10^{20}$	$1 \times 10^{19}$	$1.79 \times 10^{19}$	$2.2 \times 10^{18}$	$2.8 \times 10^{19}$	$2 \times 10^{19}$	$1.6 \times 10^{19}$	$1 \times 10^{19}$	$9 \times 10^{18}$
$N_V$ (cm <sup>-3</sup> )	$1.8 \times 10^{19}$	$1.8 \times 10^{19}$	$2 \times 10^{21}$	$1 \times 10^{19}$	$2.51 \times 10^{19}$	$1.8 \times 10^{19}$	$1 \times 10^{19}$	$1 \times 10^{19}$	$5.4 \times 10^{19}$	$1 \times 10^{19}$	$9 \times 10^{18}$
$\mu_n/\mu_p$ (cm <sup>2</sup> V <sup>-1</sup> s <sup>-1</sup> )	100/25	10/5	100/25	12/12	25/25	$2 \times 10^{-4}/2 \times 10^{-4}$	100/43.9	8600/200	50/50	20/10	25/100
$\chi$ (eV)	4	4.4	3.5	4.24	1.7	2.2	2.1	3.4	3.93	4	4.32
$E_g$ (eV)	3.3	3.35	4.6	3.1	3.6	3.0	3.1	2.2	1.55	3.2	1.4
$N_A$ (cm <sup>-3</sup> )	—	—	—	—	$5 \times 10^{18}$	$1 \times 10^{18}$	$1 \times 10^{18}$	$1 \times 10^{18}$	—	—	—
$N_D$ (cm <sup>-3</sup> )	$1 \times 10^{18}$	$1 \times 10^{18}$	$1 \times 10^{21}$	$5 \times 10^{18}$	—	—	—	—	$5 \times 10^{18}$	$3 \times 10^{18}$	—
$\tau_n/\tau_p$ (ns)	0.03/0.03	0.03/0.03	5/2	2/2	5/5	0.1/0.1	3/3	3/3	8/8	5/2	2.4/2.4
Ref.	54	55	56 and 57	58–61	56	56 and 62	56 and 63	64 and 65	62 and 64	66	67

metal contact, surface recombination is also considered for the simulation. The surface recombination velocity is set at  $1 \times 10^7 \text{ cm s}^{-1}$  for both electrons and holes.

## 2.2. Simulation details

The materials' complex refractive indices ( $n$  and  $k$ ) are plotted in Fig. S3, S5† and 7g. Also, the electrical parameters of the solar cell's layers (ZnO, AZO, CeO<sub>2</sub>, TiO<sub>2</sub>-Graphen (5%) (TiGO-5), CuSCN, Spiro-OMeTAD, CuI, Cu<sub>2</sub>O, MAPbI<sub>3</sub>, TiO<sub>2</sub>, MoSe<sub>2</sub>),

including:  $\epsilon$ ,  $N_C$ ,  $N_V$ ,  $\mu_n$ ,  $\mu_p$ ,  $\chi$ ,  $E_g$ ,  $N_A$ ,  $N_D$ ,  $\tau_n$  and  $\tau_p$  are provided in Table 1.

## 3. Results and discussion

### 3.1. Metasurface based reflector design

Fig. 2 shows the schematic of different types of structures in solar cells. The common inverted solar cell structures, as depicted in Fig. 2a, typically use bulk TiO<sub>2</sub> as ETL on the contact. To enhance the reflection from the TiO<sub>2</sub> surface, metasurface structures can be utilized. Unlike the natural behavior of materials, metasurface structures exhibit unique physical properties. Fig. 2b illustrates a reflector structure consisting of Al on SiO<sub>2</sub> (as anti-reflection coating) substrate. Also, Fig. 2c shows the structure when the bulk TiO<sub>2</sub> is applied on Al and SiO<sub>2</sub>. Finally, the schematic of the proposed metasurface unit cell consisting of TiO<sub>2</sub> nanocubes on the Al and SiO<sub>2</sub> substrate is presented in Fig. 2d. TiO<sub>2</sub> is a preferred material for solar cell structures due to its high refractive index, smooth surface, and low heat loss, particularly in the visible region. The dimensions of the TiO<sub>2</sub> nanocubes, including length ( $L$ ), width ( $W$ ), and height ( $H$ ), are represented by specific parameters. Additionally, the angle of the nanocubes relative to the horizontal axis is shown with the parameter  $\alpha$ . Based on the results, it can be argued that the use of TiO<sub>2</sub> nanocubes on Al and SiO<sub>2</sub> substrate can improve the efficiency of photonic structures and solar cells

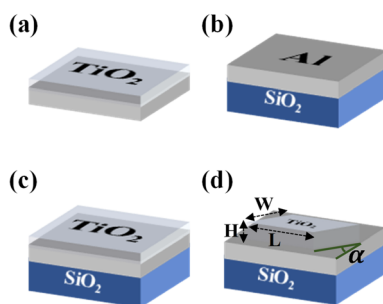


Fig. 2 (a) A common structure used as ETL in solar cells. (b) A reflector consisting of Al and SiO<sub>2</sub>. (c) The common structure of ETL in solar cells on SiO<sub>2</sub> substrate. (d) TiO<sub>2</sub>/Al/SiO<sub>2</sub> metasurface reflector structure.

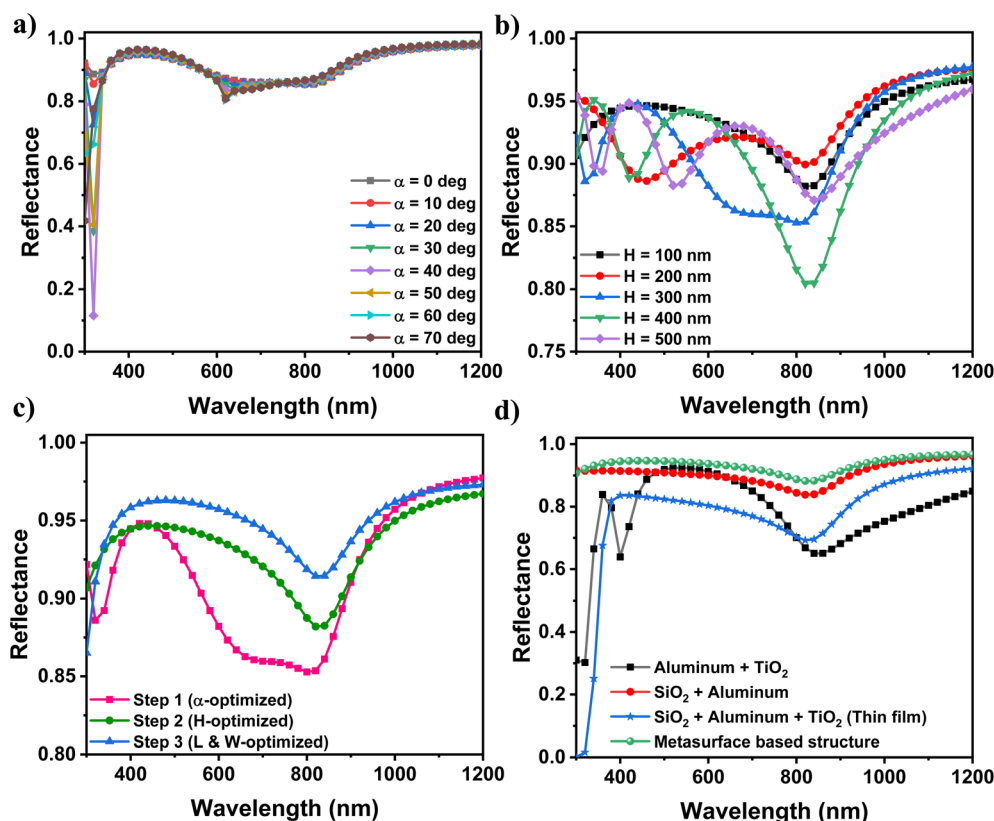


Fig. 3 The reflectance spectrum in terms of wavelength in the range of 300 to 1200 nm for (a) different values of  $\alpha$  (nanocubic angle with horizontal axis), while considering  $H = 300 \text{ nm}$ ,  $L = 150 \text{ nm}$ , and  $W = 90 \text{ nm}$ , (b) different values of  $H$ , while considering  $\alpha = 0$ ,  $L = 150 \text{ nm}$ , and  $W = 90 \text{ nm}$ , (c) different optimizations including three steps, (d) comparing the optimized metasurface structure with other structures in Fig. 2.



by enhancing the reflection from the  $\text{TiO}_2$  surface. The height of the Al and  $\text{SiO}_2$  substrate is 150 nm and 300 nm, respectively, while the length and width of the unit cell are both equal to 250 nm. Opting the mentioned dimensions serves two purposes: first, the unit cell's dimensions must be smaller than the incident wavelength, and second, the structure must be easily manufactured, particularly through electron beam lithography. The main objective of designing the proposed metasurface structure is to develop a reflector that reflects the transmitted light through the structure, to increase the total absorption in the structure.

Each of the structures shown in Fig. 2 behaved differently to electromagnetic waves, and consequently, the amount of

**Table 2** Reflectance values for (a) different values of  $\alpha$  considering  $H = 300$  nm,  $L = 150$  nm and  $W = 90$  nm, (b) different values of  $H$  considering  $\alpha = 0^\circ$ ,  $L = 150$  nm and  $W = 90$  nm, (c) different values of  $L$  considering  $\alpha = 0^\circ$ ,  $H = 100$  nm and  $L/W = 15/9$ , and (d) different provided structures in Fig. 2

(a)		
$H/L/W$ (nm)	$\alpha^\circ$	Reflectance (%)
300/150/90	0	91.57
300/150/90	10	91.50
300/150/90	20	91.20
300/150/90	30	90.46
300/150/90	40	89.83
300/150/90	50	90.46
300/150/90	60	91.06
300/150/90	70	91.16
(b)		
$\alpha^\circ/L/W$ (nm)	$H$ (nm)	Reflectance (%)
0/150/90	100	93.36
0/150/90	200	92.97
0/150/90	300	91.57
0/150/90	400	91.11
0/150/90	500	91.81
(c)		
$\alpha^\circ/H$ (nm)	$L$ (nm)	Reflectance (%)
0/100	90	91.82
0/100	110	92.29
0/100	130	92.82
0/100	150	93.36
0/100	170	93.90
0/100	190	94.47
0/100	210	94.20
(d)		
Structures	Reflectance (%)	
Fig. 1a	78.08	
Fig. 1b	90.64	
Fig. 1c	77.35	
Fig. 1d	94.47	

reflection from each structure varied. To increase the amount of reflectance from the reflector surface, various parameters, including  $H$ ,  $L$ ,  $W$ , and  $\alpha$  were optimized. Therefore, the angle of the nanocube with the  $X$ -axis, represented by the parameter  $\alpha$ , was swept from  $0^\circ$  to  $70^\circ$  with steps of  $10^\circ$  to. According to Fig. 3a and Table 2, a, and the incident power has the highest amount of reflection in the structure, reaching 91.57%, when the angle is  $0^\circ$ . The  $H$ ,  $L$  and  $W$  parameters of the  $\text{TiO}_2$  nanocubes are also effective in determining the amount of reflectance of the structure. By examining different heights of nanocubes from 100 to 500 nm with steps of 100 nm, different results were obtained. As the height was increased, the amount of reflectance from the surface decreased, and the highest amount of reflectance from the structure was at  $H = 100$  nm according to Table 2, b. This could be explained by the frequency shift in the reflectance spectrum, where it reached the highest amount of reflection in the wavelength range of 300 to 1200 nm at this height. The amount of reflectance was increased to 93.36% by optimizing the height, which is more efficient compared to when the angle was optimized, 91.57%. Then, the  $L$  parameter was varied from 90 nm to 210 nm with steps of 20 nm while keeping the angle and height constant at their optimized values. The best result was obtained at  $L = 190$  nm, which increased the amount of reflection up to 94.47% compared to the height optimization. The ratio of  $L/W$  was considered equal to 15/9. The optimal dimensions of the  $\text{TiO}_2$  nanocubes were determined to be  $\alpha = 0^\circ$ ,  $H = 100$  nm, and  $L = 190$  nm. By optimizing these parameters, the total reflectance of the structure in the wavelength range of 300 to 1200 nm reached a significant amount of 94.47%. The amount of reflection from the surface of the depicted structures in Fig. 2, is displayed in Fig. 3d. The metasurface structure exhibited a significant increase in reflectance compared to other structures, particularly the structure in Fig. 2a, which is commonly used in solar cells. According to Table 2, d, the amount of reflection in the wavelength range of 300 to 1200 nm in the provided metasurface structure in Fig. 2d was significantly increased from 78.08% to 94.47% compared to the given structure in Fig. 2a, which is commonly used in solar cells.

In order to enhance the light reflectance, other shapes of metasurface structures with  $\text{TiO}_2$  was further investigated. The depicted nanocubic structure in Fig. 2a, proved to reflect 94.47% of the incident light power. According to Fig. 4e, the provided structures in Fig. 4b-d shared higher values of light reflectance equal to 95.83%, 96.52%, and 97.95%, respectively. It was apparent that the  $\text{TiO}_2$  nanodiscs structure with the height of 100 nm and the diameter of 190 nm was selected as the most efficient structure for additional studies. Plus, the  $\text{TiO}_2$  nanodiscs have proven transfer electrons more effectively. Fig. 4e displays the reflectance diagram of the reflector structure in terms of wavelength in the range of 300 to 1200 nm, when using different types of nanocubes and nanodiscs as depicted in Fig. 4a-d. After rigorous examination, it was discovered that the materials' refractive indices, which surrounds the nano-structures, had a noticeable impact on the amount of the reflectance from the metasurface-based reflector structure. As



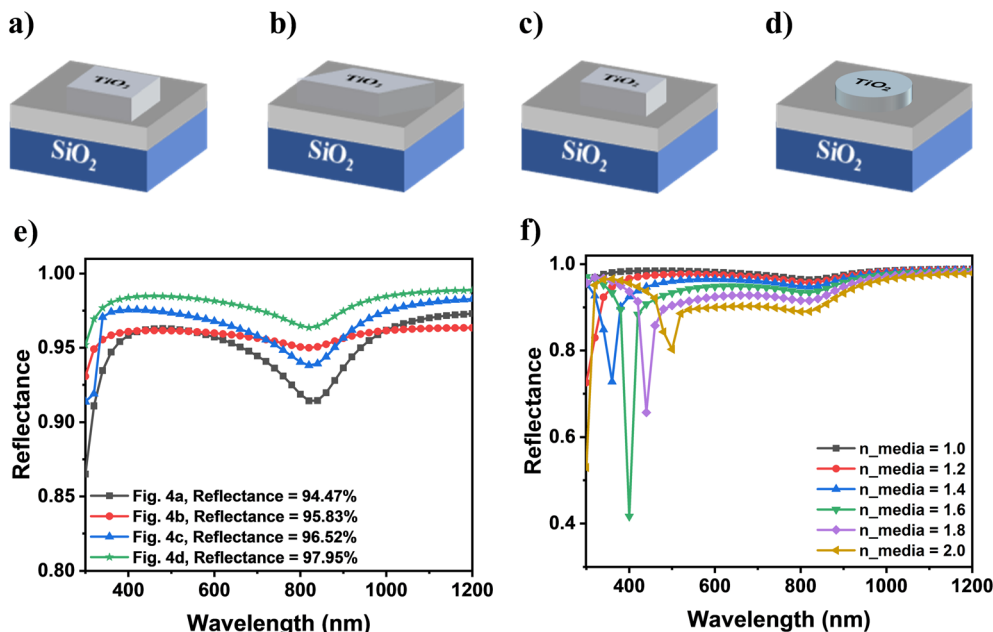


Fig. 4 The schematic of the metasurface reflector nanostructure with (a–c) three different types of nanocubes and (d) nanodisks. (e) The reflectance spectrum of the depicted nanostructures in (a–d). (f) The reflectance spectrum for the metasurface reflector considering different refractive indices values (1 to 2 with steps of 0.2) for the media around the  $\text{TiO}_2$  nanodisks.

illustrated in Fig. 4f, by changing the refractive index of the media around the  $\text{TiO}_2$  nanodisks, the reflectance from the structure was changed. The investigated refractive index range was from 1 to 2 with steps of 0.2. According to the obtained results, the amount of reflection was higher in medias with lower refractive indices, which suggested that using materials with low refractive indices would result in more light absorption in the active layer of the solar cells. In conclusion, it can be claimed that photonic and metasurface nanostructures would improve the light absorption, ease fabrication, and improve efficiency in solar cells.

The purpose of designing the  $\text{TiO}_2/\text{Al}/\text{SiO}_2$  reflector structure is to reflect light in order to reuse it in various applications such as solar cells and optical coatings. The combination of the mentioned materials allows for high reflectance at certain wavelengths. However,  $\text{TiO}_2$  has better reflective properties than other materials due to its higher dielectric constant, which leads to a higher refractive index and results in absorbing the incoming light less. Fig. S1† shows the electric field distribution of the reflector structure for three various wavelengths of 360, 500, and 740 nm. It should be pointed out that a metasurface-based reflector can exhibit resonance, when a surface is located around one of the coupled resonance frequencies. Resonance in metasurface reflectors can be reached through various methods. Moreover, it is used to achieve total reflection or design tunable metasurface unit cells. Fig. S1† depicts the three different resonances that occurred in different wavelengths, which can cause the electric field to intensify around and above the nanodisks, leading to an increase in the total absorption of the solar cell (refer to the ESI† for more details).

### 3.2. Solar cell design

It is worth noting that the refractive index of the upper layer of  $\text{TiO}_2$  nanodisks has an impact on the reflection spectra from this layer. To investigate this effect, the refractive index of this layer was swept from 1 to 4 with steps of 0.5, assuming the extinction coefficient to be equal to zero, which means no light absorption. By calculating the absorptance spectra from the surface of these layers, as provided in Fig. 5b, it was found that the refractive index range of 2 to 3 has the highest amount of light absorption in the structure. It is generally acknowledged that the enhancement in the reflectance spectra from the ETL can increase the light absorption in the active layer in an inverted solar cell. Plus, it prevents power loss by the metal contact. The finally proposed solar cell structure is presented in Fig. 5a. The structure is consisted of the following layers from top to bottom: ITO, HTL, active layer ( $\text{MAPbI}_3$ ), ETL including  $\text{TiO}_2$  nanodisks and the other bulk material around these nanodisks, Al, and  $\text{SiO}_2$ . ITO was used as a transparent contact for light to pass through. The band diagram of the proposed solar cell in the presence of the metasurface reflector is illustrated in Fig. 5c. In this structure,  $\text{ZnO}$  was used as the material around the  $\text{TiO}_2$  nanodisks, and  $\text{CuSCN}$  was used as the HTL. As plotted in Fig. 4f, the refractive index of the material around the  $\text{TiO}_2$  nanodisks did not have a significant effect on the reflectance spectra. Therefore, a material featuring a better carrier transfer should be used along with  $\text{TiO}_2$ , which can improve electron transfer, in addition to reflection improvement. According to Table 1, the  $\text{MAPbI}_3$  layer has an electron affinity of 3.93 eV and a bandgap of 1.55 eV, which can result in efficient light absorption in the wavelength range of 300 to 800 nm. On the ETL side,  $\text{TiO}_2$  and  $\text{ZnO}$  were used with the equal electron



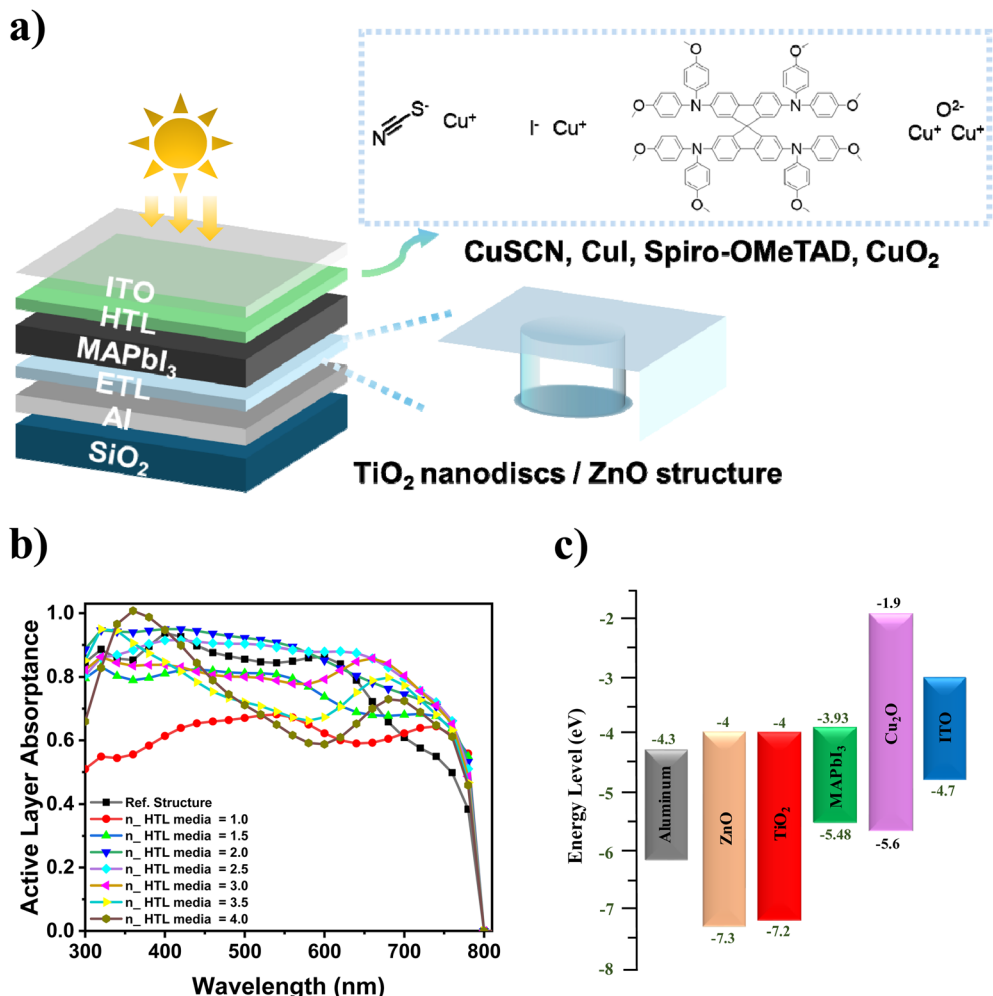


Fig. 5 (a) Schematic of the proposed solar cell with  $\text{MAPbI}_3$  as the active layer. (b) The active layer ( $\text{MAPbI}_3$ ) light absorptance spectrum with different HTL refractive indices between the range of 1 to 4 with steps of 0.5, while  $k = 0$ , and  $\text{ZnO}$  an  $\text{TiO}_2$  nanodiscs as ETL. (c) Band diagram of the proposed structure, considering  $\text{ZnO}$  as the material around the  $\text{TiO}_2$  nanodiscs,  $\text{MAPbI}_3$  as active layer, and  $\text{CuSCN}$  as the HTL (all energy levels depicted in this diagram are based on the values listed in Table 1).

affinity value of  $-4$  eV and the bandgap values of  $3.2$  eV and  $3.3$  eV, respectively. Due to the values of their conduction bands, these materials were able to transfer the electrons from the active layer into the Al contact with the work function of  $-4.3$  eV. Furthermore, due to the values of their valence bands compared to  $\text{MAPbI}_3$ , they prevented the holes from entering the Al contact conveniently. On the HTL side,  $\text{CuSCN}$  was used with a bandgap of  $3.4$  eV, which does not absorb a noticeable portion of light in the visible region. Therefore, most of the incident light was able to reach the active layer.  $\text{CuSCN}$  with an electron affinity of  $1.9$  eV was considered as a suitable barrier to prevent the electrons from entering the transparent contact (ITO) and transferred the generated holes in the active layer into the ITO side with a valence band energy level difference of  $0.18$  eV with  $\text{MAPbI}_3$ .

It is obvious that applying different materials around  $\text{TiO}_2$  nanodiscs can affect the amount of electron transfer. Although, according to the findings pertinent to Fig. 4f, different refractive indices did not have a significant effect on the amount of light reflection, the light transmission of these materials was

significant since they were not considered as absorbent materials. Therefore, various materials were considered for this purpose, including  $\text{ZnO}$ ,  $\text{AZO}$ ,  $\text{CeO}_2$ , and  $\text{TiGO-5}$ . The refractive indices and extinction coefficients of these materials in terms of wavelength in the range of  $300$  to  $800$  nm are shown in Figs. S2.†

As demonstrated in Fig. 6a, the absorptance spectra of the active layer ( $\text{MAPbI}_3$ ) for different materials around the  $\text{TiO}_2$  nanodiscs did not change significantly in the wavelength range of  $300$  to  $800$  nm and is almost the same for different materials, including  $\text{ZnO}$ ,  $\text{AZO}$ ,  $\text{CeO}_2$ , and  $\text{TiGO-5}$ . In order to generate electron-hole pairs, a photon with sufficient energy must be absorbed in the active layer. Therefore, the amount of carrier generation rate in different wavelengths, as depicted in Fig. 6b, is in accordance with the behavior of the absorptance diagram. Fig. 6c indicates the photocurrent density in terms of the voltage, where different values of the  $V_{oc}$ , can be explained by the different electrical characteristics of the materials. Bearing in mind that  $\text{ZnO}$  has a higher electron mobility compared to other materials, as stated in Table 1, as well as the  $0.3$  eV difference in its conduction band energy compared to the Al

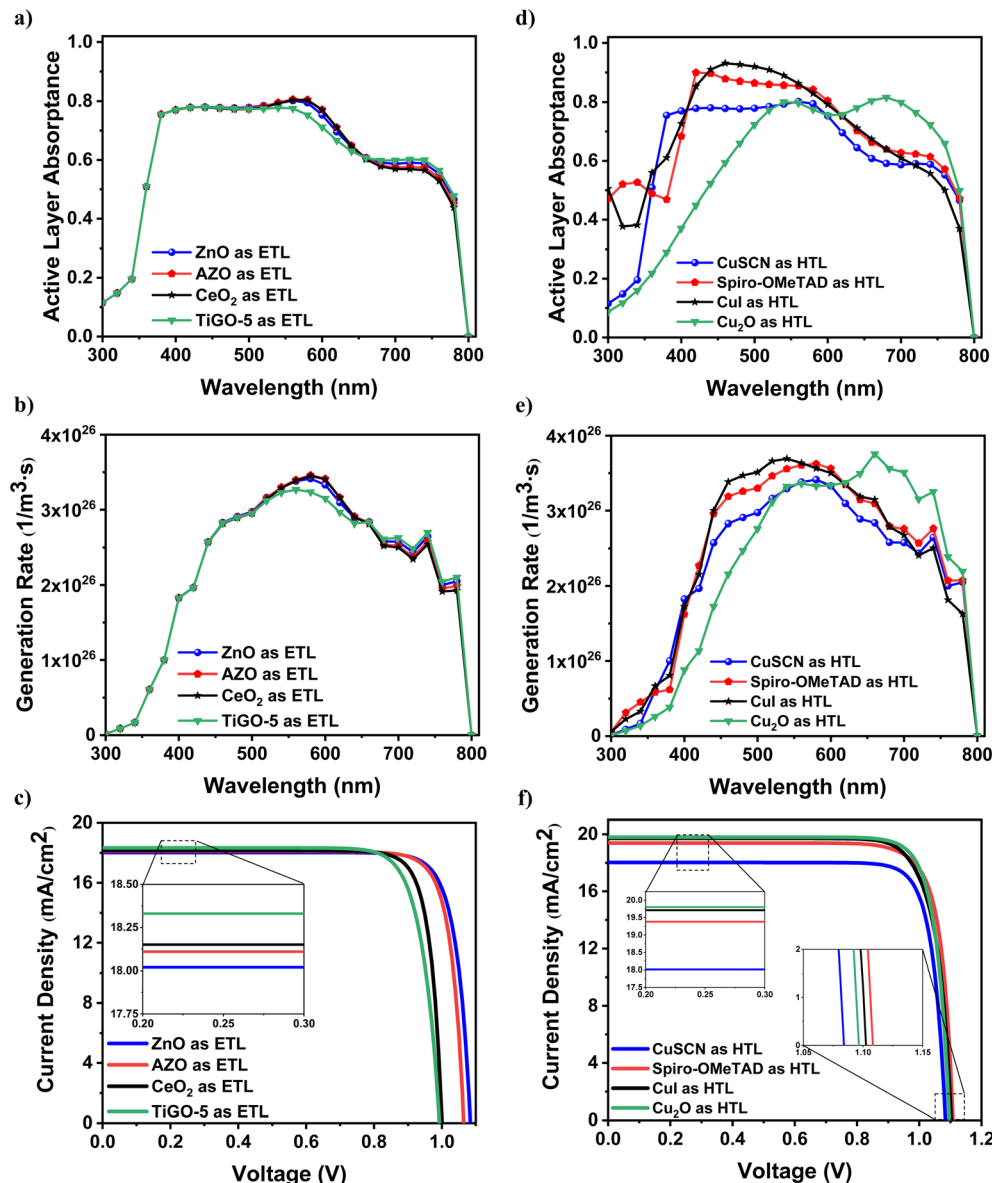


Fig. 6 The active layer (a) absorptance spectra, and (b) carrier generation rate in terms of wavelength, and (c) the photocurrent density in terms of voltage for the metasurface structure with different ETL materials around the  $\text{TiO}_2$  nanodiscs. The active layer (d) absorptance spectra, and (e) carrier generation rate in terms of wavelength, and (f) the photocurrent density in terms of voltage for the metasurface structure with different HTL materials and ZnO as ETL.

work function, it resulted in a higher  $V_{\text{oc}}$  value. Likewise, according to Table 1, AZO shared almost the same  $V_{\text{oc}}$  value as ZnO due to their approximately equal electrical parameters. Despite ZnO and AZO,  $\text{CeO}_2$  showed a relatively lower  $V_{\text{oc}}$  due to its lower conduction band than the Al work function. Similarly, TiGO-5 shared about the same  $V_{\text{oc}}$  value to  $\text{CeO}_2$ . This was because of the almost very close energy level of the TiGO-5 conduction band to the Al work function. The represented band diagram in Fig. S3<sup>†</sup> indicates that all the proposed materials as ETL can easily separate the electron from the active layer due to the lower energy level of their conduction band compared to the active layer's conduction band. Also, the holes were prevented to transfer into the metal contact in light of the same reason. It should be mentioned that the difference in  $V_{\text{oc}}$

values is mainly contributed to the difference in the conduction band of these materials with the Al work function and also the electrical parameters of these materials according to Table 1.

Table 3 The values for photovoltaic parameter including  $J_{\text{sc}}$ ,  $V_{\text{oc}}$ , PCE and FF for solar cells with  $\text{TiO}_2$  nanodiscs embedded in various ETLs

ETL materials around the $\text{TiO}_2$ nanodiscs	$J_{\text{sc}}$ ( $\text{mA cm}^{-2}$ )	$V_{\text{oc}}$ (V)	PCE (%)	FF
ZnO	18.02	1.08	16.40	0.84
AZO	18.11	1.06	16.25	0.84
$\text{CeO}_2$	18.15	1.00	15.37	0.85
TiGO-5	18.33	0.99	14.83	0.82



Table 3 denotes the values of  $J_{sc}$ ,  $V_{oc}$ , PCE, and FF of the solar cell, when the mentioned different materials around  $\text{TiO}_2$  nanodiscs were investigated. According to Fig. 4f and S2(a),<sup>†</sup> the surface reflectance value is higher for the materials with lower refractive indices. Therefore, TiGO-5 represented the highest  $J_{sc}$  value of  $18.33 \text{ mA cm}^{-2}$ , owing to featuring the lowest refractive index among other ETL materials. However, as illustrated in Fig. 4f, the reflectance curves represented an insignificant difference for materials with different refractive indices. Also, as it was stated earlier, the structure with  $\text{ZnO}$  around  $\text{TiO}_2$  nanodiscs presented the highest  $V_{oc}$  value of  $1.08 \text{ V}$ . Correspondingly, this structure showed the highest values of PCE and FF equal to  $16.40\%$  and  $0.84$ , respectively.

According to Fig. 5b, the refractive indices of HTL materials appeared to have a striking impact on the amount of the active layer's light absorption. More particularly, materials with refractive indices between  $2$  to  $3$  showed the highest amount of light absorption by the active layer. Hence, it was concluded that the light interaction between the HTL and  $\text{MAPbI}_3$  played an effective role in the amount of light reflection from the surface they shared and the proportion of the light that reached the active layer. In this regard, materials with different refractive indices were selected as HTL. These materials include CuSCN, Spiro-OMeTAD, CuI, and  $\text{Cu}_2\text{O}$ . Among these materials, the refractive indices of CuI and  $\text{Cu}_2\text{O}$  were in the target range. The refractive indices and extinction coefficients of these materials are shown in Fig. S4.<sup>†</sup> It was also observed that  $\text{Cu}_2\text{O}$  features a high extinction coefficient at lower wavelengths, which reduced the amount of active layer's light absorption at lower wavelengths.

The light reflection and absorption properties of a material can be described from its complex refractive index. The proportion of the transmitted light through the ITO and HTL layers and the reflected light from the layers below the active layer are considered as effective factors in the light absorption of the active layer. It was also distinguished earlier that employing materials with refractive indices in the range of  $2$  to  $3$  can increase the light reflection from the metasurface-based reflectors. Therefore, different HTL materials can cause different light absorption spectrum in the active layer. Fig. 6d shows the light absorptance curve of the active layer for different HTLs. Among the applied materials as HTL, CuI and  $\text{Cu}_2\text{O}$ , with refractive indices in the range of  $2$  to  $3$  in the visible light spectrum, the active layer experienced the highest light absorption in the wavelength range below  $600 \text{ nm}$ , and above  $600 \text{ nm}$ , respectively. According to Fig. 4b, the HTL medias with lower refractive indices resulted in lower light absorption spectrum in the active layer, and since the HTLs were assumed to absorb no light, this can be explained by the lower light reflection from the metasurface reflectors. Therefore, the HTL medias with lower refractive indices proved to effect on the light reflection from the metasurface reflectors. This is why the light absorption of the active layer was lower when CuSCN and Spiro-OMeTAD were employed as HTLs (Fig. 4d). Also, Fig. 6e shows the carrier generation rate of the active layer for different HTL materials. For the wavelengths below  $600 \text{ nm}$ , the light absorptance was the highest, when CuI was used as HTL, which is also evident in the carrier

generation rate diagram. For the wavelengths above  $600 \text{ nm}$ , the carrier generation rate was the highest when  $\text{Cu}_2\text{O}$  was used as HTL due to the significant light absorption of the active layer. In view of the fact that the carrier generation rate has a direct relation with  $J_{sc}$ , Fig. 6f, illustrates the highest  $J_{sc}$  values for the structures with  $\text{Cu}_2\text{O}$  and CuI as HTLs. Conversely, the structure with CuSCN as HTL represented the lowest  $J_{sc}$  value, which is due to its low refractive index and the noticeable light reflection reduction from the metasurface reflector. However, the  $V_{oc}$  values for different HTLs remained almost constant because the materials were all capable of effectively separating holes from the active layer and preventing the electrons from entering ITO contact. This can be explained through the energy band diagram of the HTLs, which are shown in Fig. S5.<sup>†</sup> The mentioned HTLs, also known as electron-blocking layers, including CuSCN, Spiro-OMeTAD, CuI, and  $\text{Cu}_2\text{O}$ , performed slightly different conduction bands equal to  $2.03 \text{ eV}$ ,  $1.73 \text{ eV}$ ,  $1.83 \text{ eV}$ , and  $2.03 \text{ eV}$ , respectively, which resulted in the moderately different  $V_{oc}$ . Additionally, the HTLs' electrical parameters, such as dielectric constant, electron and hole mobility, density of state for the conduction and valence band, electron and hole life-time and concentration of p-type doping, which are given in Table 1, were considered effective, too.

Table 4 presents the values of  $J_{sc}$ ,  $V_{oc}$ , PCE, and FF for the proposed structure with different HTLs. As mentioned above, CuI and  $\text{Cu}_2\text{O}$  represented the highest values of almost the same  $J_{sc}$  equal to  $19.71 \text{ mA cm}^{-2}$  and  $19.80 \text{ mA cm}^{-2}$ , respectively. Although the  $V_{oc}$  values did not change significantly, the Spiro-OMeTAD held the highest value equal to  $1.11 \text{ V}$ , due to its electrical characteristics. Nevertheless, the  $\text{Cu}_2\text{O}$  reported the highest value of PCE among other HTLs, equal to  $18.15\%$ , with the FF value of  $0.83$ . Comparing the values in Tables 2 and 3, the PCE value was increased by  $1.75\%$ , when the HTL was changed from CuSCN to  $\text{Cu}_2\text{O}$ .

In order to enhance the light absorption, a second absorbent layer,  $\text{MoSe}_2$ , was introduced.  $\text{MoSe}_2$  with a bandgap of  $1.4 \text{ eV}$  can absorb light in higher wavelengths compared to  $\text{MAPbI}_3$ . The  $\text{MoSe}_2$  absorption range is from  $300$  to  $920 \text{ nm}$ , as provided in Fig. S6(b).<sup>†</sup> However, employing materials with higher refractive indices, around the  $\text{TiO}_2$  nanodiscs did not have a critical impact on the light reflection from the surface of the metasurface reflector, as shown in Fig. 4f. Therefore,  $\text{MoSe}_2$  can be used around the  $\text{TiO}_2$  nanodiscs. The refractive indices and extinction coefficients of the other materials, including  $\text{MAPbI}_3$ , ITO, and  $\text{TiO}_2$ , are depicted in Fig. S6.<sup>†</sup>

The planar reference structure, as shown in Fig. 7a, from top to bottom was composed of ITO as a transparent contact,

**Table 4** The values for photovoltaic parameter including  $J_{sc}$ ,  $V_{oc}$ , PCE and FF for solar cells with various HTLs

HTL materials	$J_{sc}$ ( $\text{mA cm}^{-2}$ )	$V_{oc}$ (V)	PCE (%)	FF
CuSCN	18.02	1.08	16.40	0.84
Spiro-OMeTAD	19.38	1.11	17.74	0.82
CuI	19.71	1.10	17.73	0.80
$\text{Cu}_2\text{O}$	19.80	1.09	18.15	0.83



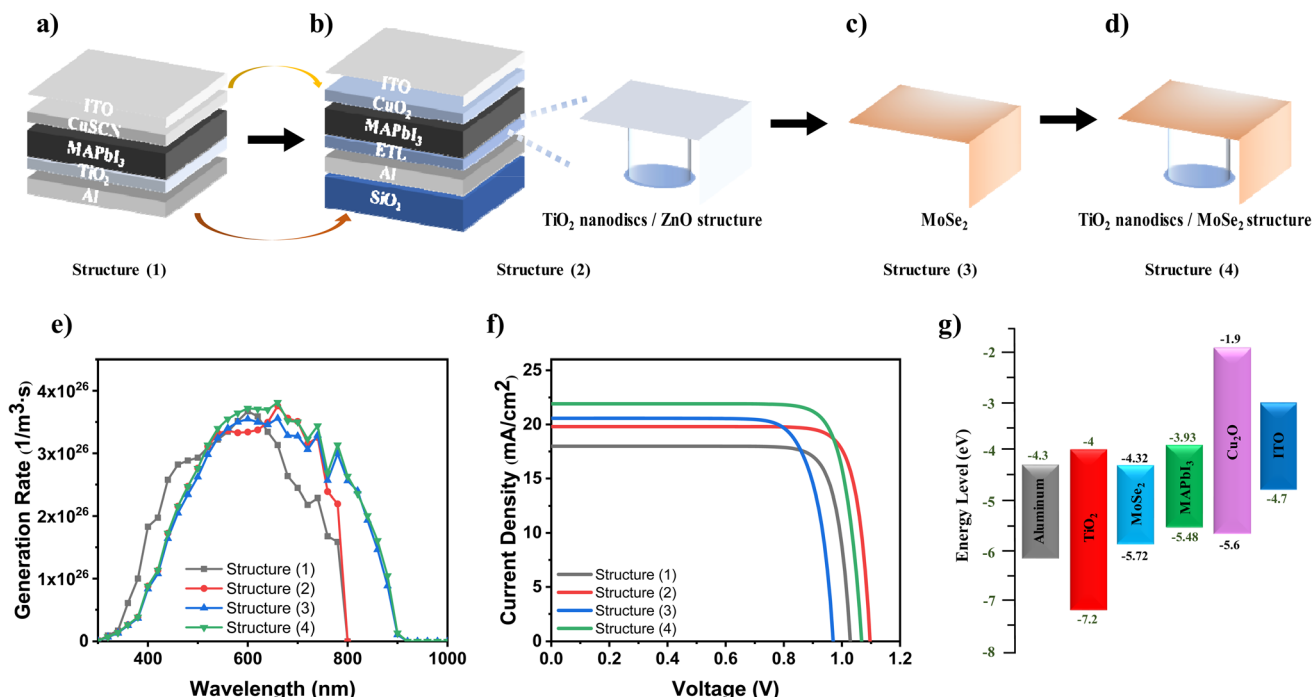


Fig. 7 The device architecture for (a) the planar reference structure (structure (1)), (b) the proposed metasurface-based structure with ZnO around the TiO<sub>2</sub> nanodiscs as ETL, and Cu<sub>2</sub>O as HTL (structure (2)), (c) the planar structure with MoSe<sub>2</sub> as ETL and the second absorber, and Cu<sub>2</sub>O as HTL (structure (3)), and (d) the metasurface-based structure with MoSe<sub>2</sub> around TiO<sub>2</sub> nanodiscs as the second absorber, and Cu<sub>2</sub>O as HTL (structure (4)). The (e) carrier generation rate in terms of wavelength, and (f) current density in terms of voltage for the provided structures 1 to 4. (g) Band diagram of the structure 4 (all energy levels depicted in this diagram are based on the values listed in Table 1).

CuSCN as the HTL, MAPbI<sub>3</sub> as the active layer, TiO<sub>2</sub> as the ETL, and Al as the metal contact. Finally, four main structures were investigated, which can be explained as: (1) the planar reference structure (Fig. 7a), (2) the proposed metasurface-based structure with ZnO around the TiO<sub>2</sub> nanodiscs as ETL, and Cu<sub>2</sub>O as HTL (Fig. 7b), (3) the planar structure with MoSe<sub>2</sub> as ETL and the second absorber, and Cu<sub>2</sub>O as HTL (Fig. 7c), and (4) the metasurface-based structure with MoSe<sub>2</sub> around TiO<sub>2</sub> nanodiscs as the second absorber, and Cu<sub>2</sub>O as HTL (Fig. 7d). The presence of TiO<sub>2</sub> nanodiscs can improve the efficiency of the system in two ways: (1) creating a metasurface reflector to increase the light reflection from the lower surface of the active layer to increase the  $J_{sc}$  value, and (2) improving the electron transfer through the nanodiscs, which increases  $V_{oc}$ . According to Fig. 7e, the carrier generation rate was higher in the structure (4) compared to the other structures owing to the presence of both the MoSe<sub>2</sub> as the second absorber layer and the TiO<sub>2</sub> nanodiscs. The increase in the carrier generation rate, resulted in an increase in the  $J_{sc}$  value. According to Fig. 7f, which demonstrates the current density curves in terms of voltage, the  $J_{sc}$  value of the structure (4) is higher than the other structures due to the smaller bandgap of MoSe<sub>2</sub> compared to MAPbI<sub>3</sub>, which absorbs light with wavelengths greater than 800 nm in the infrared region, as well as the higher light reflectance caused by the TiO<sub>2</sub> nanodiscs. Utilizing the TiO<sub>2</sub> nanodiscs along with ZnO in the structure (2) enhanced the carrier transfer rate, where both materials acted as hole blockers in the system.

Therefore, the  $V_{oc}$  value was increased slightly more than the other structures. On this account, structure (2) held a higher  $V_{oc}$  value compared to structures (3 and 4) in light of the lack of proper hole blocking in MoSe<sub>2</sub>, which consequently increased the carrier recombination rate. Fig. 7g presents the energy band diagram related to the metasurface-based structure, where the TiO<sub>2</sub> nanodiscs were surrounded by the MoSe<sub>2</sub>. In order to further discuss the lower  $V_{oc}$  of the structures (3 and 4), the electrical properties of MoSe<sub>2</sub> were studied. As indicated in Table 1, MoSe<sub>2</sub> has an electron affinity equal to 4.32 eV and a bandgap equal to 1.4 eV. As a consequence of the lower energy level of the conduction band in MoSe<sub>2</sub> compared to MAPbI<sub>3</sub>, the generated electrons in MAPbI<sub>3</sub> layer were able to be transferred

Table 5 Comparison of the  $J_{sc}$ ,  $V_{oc}$ , PCE and FF values for different structures of: (1) the planar reference structure, (2) the proposed metasurface-based structure with ZnO around the TiO<sub>2</sub> nanodiscs as ETL, and Cu<sub>2</sub>O as HTL, (3) the planar structure with MoSe<sub>2</sub> as ETL and the second absorber, and Cu<sub>2</sub>O as HTL, and (4) the metasurface-based structure with MoSe<sub>2</sub> around TiO<sub>2</sub> nanodiscs as the second absorber, and Cu<sub>2</sub>O as HTL

Structure	$J_{sc}$ (mA cm <sup>-2</sup> )	$V_{oc}$ (V)	PCE (%)	FF
1	17.98	1.03	15.33	0.84
2	19.80	1.09	18.15	0.83
3	20.56	0.97	15.75	0.78
4	21.91	1.07	19.17	0.82



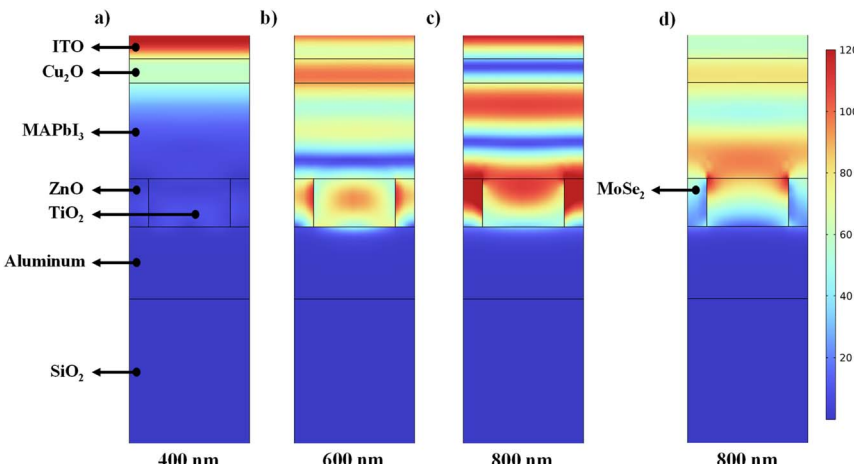


**Fig. 8** Distribution of the electric field for the single junction metasurface reflector at different wavelengths of (a) 400 nm, (b) 600 nm, and (c) 800 nm. (d) Distribution of the electric field for the structure in the presence of  $\text{MoSe}_2$  as the second absorbent layer at the wavelength of 800 nm.

into the metal contact, which resulted in lower  $V_{\text{oc}}$  values of the structures (3 and 4) compared to structure (2). However, the lower energy level of the valence band in  $\text{MoSe}_2$  compared to  $\text{MAPbI}_3$ , was beneficial as it prevented the generated holes in  $\text{MAPbI}_3$  from entering the metal contact and transferring the generated holes in  $\text{MoSe}_2$  into the  $\text{MAPbI}_3$ .

Table 5 displays the values of the  $J_{\text{sc}}$ ,  $V_{\text{oc}}$ , PCE, and FF for the structures (1 to 4). The  $J_{\text{sc}}$  value was enhanced from  $19.80 \text{ mA cm}^{-2}$  to  $21.91 \text{ mA cm}^{-2}$ , when the  $\text{MoSe}_2$  was applied into the structure (2) instead of the  $\text{ZnO}$ . However, as a result of the better electron transfer and hole blocking in the  $\text{ZnO}$  layer compared to  $\text{MoSe}_2$ , the value of the  $V_{\text{oc}}$  in structure (3) fell from  $1.09 \text{ V}$  to  $1.07 \text{ V}$  compared to structure (2). Accordingly, the total PCE value was increased from  $18.15\%$  to  $19.17\%$ , when  $\text{MoSe}_2$  replaced the  $\text{ZnO}$  around the  $\text{TiO}_2$  nanodiscs. Both structures (2 and 4) were improved, comparing their electrical characteristics including  $J_{\text{sc}}$ ,  $V_{\text{oc}}$ , PCE, and FF to the planar structures (1 and 3) provided in Table 5, respectively. However, structure (4) was improved more significantly and reached the highest value of PCE equal to  $19.17\%$  as the champion structure among others. Also, the lack of optimal carrier separation in the system reduces the FF. By incorporating  $\text{MoSe}_2$  into the structure, due to its narrow band diagram, some electrons generated in the  $\text{MAPbI}_3$  layer enter the HTL. As illustrated in the band diagram of the structure (Fig. 7g), the electron entry into the HTL increases the series resistance, thereby reducing the FF. Additionally, some of these electrons recombine with the holes in the HTL, which leads to a decrease in the  $V_{\text{oc}}$  when using  $\text{MoSe}_2$ . However, considering the significant increase in  $J_{\text{sc}}$  compared to the decreases in  $V_{\text{oc}}$  and FF, it can be concluded that  $\text{MoSe}_2$  is a better choice compared to  $\text{ZnO}$ .

Fig. 8 illustrates the electric field distribution in three different wavelengths of 400, 600, and 800 nm for the structure (2) and at the wavelength of 800 nm for the structure (4). At the wavelength of 400 nm, provided in Fig. 8a, only a small percentage of the electric field entered the active layer due to

light absorption in HTL ( $\text{Cu}_2\text{O}$ ), where it absorbed approximately 30% of the input power, which is less than other materials. At the wavelength of 600 nm, according to Fig. 8b, the layers above the active layer (ITO and  $\text{Cu}_2\text{O}$ ) showed no light absorption. In fact, Fig. S4(b) and S6(b)† indicate that most of the sunlight reached the active layer. About 75% of the incident light was absorbed in the active layer, together with the reflected light from the lower layers. Additionally, a strong electric field was formed around the  $\text{TiO}_2$  nanodiscs due to their resonances. At the wavelength of 800 nm, according to Fig. 8c, the electric field reached the ETL. Due to the light reflection from the metasurface reflector and the resonance of the electric field between the nanodiscs, a strong field was formed in the ETL as well as the lower part of the active layer. Applying  $\text{MoSe}_2$  as an absorbent material with the smaller bandgap than  $\text{MAPbI}_3$  intensified the transmitted electric field through the active layer and increased the PCE. Fig. 8d shows the electric field distribution at the wavelength of 800 nm for structure (4). Moreover, a significant portion of the electric field around the  $\text{TiO}_2$  nanodiscs that was depicted in Fig. 8c was absorbed by  $\text{MoSe}_2$  in structure (4). According to Fig. 7e, the overall light absorptance and carrier generation of structure (4) in the presence of  $\text{MoSe}_2$  at the wavelength of 800 nm seemed to have a significant portion, while for structure (2), this value is zero at this wavelength.

## 4. Conclusion

The efficiency of an inverted perovskite solar cell using a new perfect metasurface-based reflector with  $\text{TiO}_2$  nanodiscs/ $\text{MoSe}_2$  structure as ETL was enhanced through several optimizations. Initially, the perfect metasurface-based reflector structure ( $\text{TiO}_2/\text{Al}/\text{SiO}_2$ ) was investigated and compared in different types of nanostructures, including: four different nanocubes and nanodiscs structures. It was explored that using  $\text{TiO}_2$  as nanodiscs compared to  $\text{TiO}_2$  as a bulk layer on an Al substrate

increased the reflectance from 78.08% to 97.95%. Subsequently, the light absorption in the active layer and the carrier transfer through the structure were improved. Additionally, different materials were investigated as the ETLs around the  $\text{TiO}_2$  nanodiscs (ZnO, AZO,  $\text{CeO}_2$ , and TiGO-5), while other materials as an HTL above the active layer (CuSCN, Spiro-OMeTAD, CuI, and  $\text{Cu}_2\text{O}$ ). The optimum structure consisting of ITO/ $\text{Cu}_2\text{O}$ /MAPbI<sub>3</sub>/ $\text{TiO}_2$  nanodiscs and ZnO/Al/SiO<sub>2</sub>, obtained the values of the  $J_{sc}$ ,  $V_{oc}$ , PCE, and FF equal to  $19.80 \text{ mA cm}^{-2}$ , 1.09 V, 18.15%, and 0.83, respectively. By applying MoSe<sub>2</sub> around  $\text{TiO}_2$  nanodiscs with a smaller bandgap than the MAPbI<sub>3</sub>, as the second absorbent in the infrared region, the electrical characteristics of the cell were improved compared to the planar reference invert solar cell structure (ITO/CuSCN/MAPbI<sub>3</sub>/ $\text{TiO}_2$ /Al), where the values of the  $J_{sc}$ ,  $V_{oc}$ , and PCE were increased from  $17.98 \text{ mA cm}^{-2}$  to  $21.91 \text{ mA cm}^{-2}$ , 1.03 V to 1.07 V, and 15.33% to 19.17%, respectively.

## Data availability

The data supporting this article have been included as part of the ESI.† Additional datasets generated and analyzed during the study, including optoelectronic simulations and characterization results, can be made available upon reasonable request by contacting the corresponding author.

## Author contributions

Javad Maleki and Maryam Shahrostami: conceptualization, data curation, formal analysis, investigation, methodology, software, validation, visualization, writing – original draft, writing – review & editing. Siming Huang: investigation, validation, visualization, writing – review & editing. Mojtaba Abdi-Jalebi: conceptualization, data curation, formal analysis, funding acquisition, investigation, methodology, project administration, supervision, resources, validation, visualization, writing – review & editing.

## Conflicts of interest

The authors declare no conflict of interest.

## Acknowledgements

M. A.-J. acknowledges the Department for Energy Security and Net Zero (Project ID: NEXTCCUS), University College London's (UCL) Research, Innovation and Global Engagement, University of Sydney–University College London Partnership Collaboration Awards, Cornell-UCL Global Strategic Collaboration Awards and UCL-IITD Joint seed fund for their financial support. M. A.-J. acknowledges the ACT program (Accelerating CCS Technologies, Horizon 2020 Project No. 691712) for the financial support of the NEXTCCUS project (Project ID: 327327). M. A.-J. and S. H. acknowledge the UCL-IISc Seed Grant and UCL-Peking University Strategic Partner Fund for financial support. We wish to acknowledge the support of the Henry Royce Institute for Advanced Materials through the

Industrial Collaboration Programme (RICP-R4-100061) and MATcelerateZero (MATZ0), funded from a grant provided by the Engineering and Physical Sciences Research Council EP/X527257/1.

## References

- 1 S. Kanwal, M. T. Mehran, M. Hassan, M. Anwar, S. R. Naqvi and A. H. Khoja, An integrated future approach for the energy security of Pakistan: Replacement of fossil fuels with syngas for better environment and socio-economic development, *Renewable Sustainable Energy Rev.*, 2022, **156**, 111978.
- 2 F. A. Malla, S. A. Bandh, S. A. Wani, A. T. Hoang and N. A. Sofi, Biofuels: Potential Alternatives to Fossil Fuels, in *Biofuels in Circular Economy*, Springer, 2023, pp. 1–15.
- 3 Y. Huang, J. Lin, Y. Wang, J. Min, R. Wang, D. Jin and B. Wei, Forecast of fossil fuel demand based on low carbon emissions from the perspective of energy security, *Chem. Technol. Fuels Oils*, 2023, **58**(6), 1075–1082.
- 4 M. K. H. Rabaia, M. A. Abdelkareem, E. T. Sayed, K. Elsaid, K.-J. Chae, T. Wilberforce and A. Olabi, Environmental impacts of solar energy systems: A review, *Sci. Total Environ.*, 2021, **754**, 141989.
- 5 S. E. Hosseini and M. A. Wahid, Hydrogen from solar energy, a clean energy carrier from a sustainable source of energy, *Int. J. Energy Res.*, 2020, **44**(6), 4110–4131.
- 6 C. M. S. Kumar, S. Singh, M. K. Gupta, Y. M. Nimdeo, R. Raushan, A. V. Deorankar, T. M. A. Kumar, P. K. Rout, C. S. Chanotiya, V. D. Pakhale, *et al.*, Solar energy: A promising renewable source for meeting energy demand in Indian agriculture applications, *Sustain. Energy Technol. Assessments*, 2023, **55**, 102905.
- 7 Y. Park, B. Zhao and S. Fan, Reaching the ultimate efficiency of solar energy harvesting with a nonreciprocal multijunction solar cell, *Nano Lett.*, 2021, **22**(1), 448–452.
- 8 Z. Wu, E. Bi, L. K. Ono, D. Li, O. M. Bakr, Y. Yan and Y. Qi, Passivation Strategies for Enhancing Device Performance of Perovskite Solar Cells, *Nano Energy*, 2023, 108731.
- 9 Y.-E. Lye, K.-Y. Chan and Z.-N. Ng, A Review on the Progress, Challenges, and Performances of Tin-Based Perovskite Solar Cells, *Nanomaterials*, 2023, **13**(3), 585.
- 10 M. Haghghi, N. Ghazyani, S. Mahmoodpour, R. Keshtmand, A. Ghaffari, H. Luo, R. Mohammadpour, N. Taghavinia and M. Abdi-Jalebi, Low-Temperature Processing Methods for Tin Oxide as Electron Transporting Layer in Scalable Perovskite Solar Cells, *Sol. RRL*, 2023, **7**(10), 2201080.
- 11 M. Abdi Jalebi, The Future of Halide Perovskite Solar Cells, *Nanoscale Adv. Mater.*, 2024, **1**(2), 87–94, DOI: [10.22034/nsam.2024.04.02](https://doi.org/10.22034/nsam.2024.04.02).
- 12 D. Wang, M. Chen, X. Lei, Y. Wang, Y. Bao, X. Huang, P. Zhu, J. Zeng, X. Wang, S. Tsang, *et al.*, All-In-One Additive Enabled Efficient and Stable Narrow-Bandgap Perovskites for Monolithic All-Perovskite Tandem Solar Cells, *Adv. Mater.*, 2024, 2411677.



13 Z.-E. Shi, T.-H. Cheng, C.-Y. Lung, C.-W. Lin, C.-L. Wang, B.-H. Jiang, Y.-S. Hsiao and C.-P. Chen, Achieving over 42% indoor efficiency in wide-bandgap perovskite solar cells through optimized interfacial passivation and carrier transport, *Chem. Eng. J.*, 2024, **498**, 155512.

14 B. H. Jiang, Z. J. Gao, C. Y. Lung, Z. E. Shi, H. Y. Du, Y. W. Su, H. S. Shih, K. M. Lee, H. H. Hung, C. K. Chan, *et al.*, Enhancing the Efficiency of Indoor Perovskite Solar Cells through Surface Defect Passivation with Coplanar Heteroacene Cored A-D-A-type Molecules, *Adv. Funct. Mater.*, 2024, **34**(19), 2312819.

15 M. A. Mahmud, J. Zheng, J. F. Chang, G. Wang, C. Liao, M. H. Rahman, W. B. Tarique, S. Tang, J. Bing, C. G. Bailey, *et al.*, Halogenated Polycyclic Aromatic Hydrocarbon for Hole Selective Layer/Perovskite Interface Modification and Passivation for Efficient Perovskite-Organic Tandem Solar Cells with Record Fill Factor, *Adv. Energy Mater.*, 2024, 2400691.

16 S. Liu, Z. Sun, X. Lei, T. Miao, Q. Zhou, R. Chen, J. Wang, F. Ren, Y. Pan, Y. Cai, *et al.*, Stable Surface Contact with Tailored Alkylamine Pyridine Derivatives for High-Performance Inverted Perovskite Solar Cells, *Adv. Mater.*, 2024, 2415100.

17 B. Gil, A. J. Yun, J. Lim, J. Cho, B. Kim, S. Ryu, J. Kim and B. Park, Design of SnO<sub>2</sub> Electron Transport Layer in Perovskite Solar Cells to Achieve 2000 h Stability Under 1 Sun Illumination and 85 °C, *Adv. Mater. Interfaces*, 2023, **10**(11), 2202148.

18 A. A. Said, J. Xie and Q. Zhang, Recent progress in organic electron transport materials in inverted perovskite solar cells, *Small*, 2019, **15**(27), 1900854.

19 M. Noman, M. Shahzaib, S. T. Jan, S. N. Shah and A. D. Khan, 26.48% efficient and stable FAPbI<sub>3</sub> perovskite solar cells employing SrCu<sub>2</sub>O<sub>2</sub> as hole transport layer, *RSC Adv.*, 2023, **13**(3), 1892–1905.

20 Q. Lin, D. J. Kubicki, M. Omrani, F. Alam and M. Abdi-Jalebi, The race between complicated multiple cation/anion compositions and stabilization of FAPbI<sub>3</sub> for halide perovskite solar cells, *J. Mater. Chem. C*, 2023, **11**(7), 2449–2468.

21 G. Nan, X. Zhang, M. Abdi-Jalebi, Z. Andaji-Garmaroudi, S. D. Stranks, G. Lu and D. Beljonne, How methylammonium cations and chlorine dopants heal defects in lead iodide perovskites, *Adv. Energy Mater.*, 2018, **8**(13), 1702754.

22 Q. Lin, S. P. Senanayak, N. Yaghoobi Nia, M. Alsari, S. Lilliu and M. Abdi-Jalebi, Impact of A-Site Cation Modification on Charge Transport Properties of Lead Halide Perovskite for Photovoltaics Applications, *Energy Technol.*, 2023, **11**(9), 2300358.

23 H. Li, C. Ding, D. Liu, S. Yajima, K. Takahashi, S. Hayase and Q. Shen, Efficient Charge Transfer in MAPbI<sub>3</sub> QDs/TiO<sub>2</sub> Heterojunctions for High-Performance Solar Cells, *Nanomaterials*, 2023, **13**(7), 1292.

24 D. M. Niedzwiedzki, H. Zhou and P. Biswas, Exciton binding energy of MAPbI<sub>3</sub> thin film elucidated via analysis and modeling of perovskite absorption and photoluminescence properties using various methodologies, *J. Phys. Chem. C*, 2022, **126**(2), 1046–1054.

25 T. Ouslimane, L. Et-Taya, L. Elmaimouni and A. Benami, Impact of absorber layer thickness, defect density, and operating temperature on the performance of MAPbI<sub>3</sub> solar cells based on ZnO electron transporting material, *Heliyon*, 2021, **7**(3), e06379.

26 Z. Hu, C. Liu and G. Li, Disordered optical metasurfaces: from light manipulation to energy harvesting, *Adv. Phys.:X*, 2023, **8**(1), 2234136.

27 A. S. Rana, M. Zubair, Y. Chen, Z. Wang, J. Deng, M. T. S. Chani, A. Danner, J. Teng and M. Q. Mehmood, Broadband solar absorption by chromium metasurface for highly efficient solar thermophovoltaic systems, *Renewable Sustainable Energy Rev.*, 2023, **171**, 113005.

28 M. I. Hossain, N. Yumnam, W. Qarony, A. Salleo, V. Wagner, D. Knipp and Y. H. Tsang, Non-resonant metal-oxide metasurfaces for efficient perovskite solar cells, *Sol. Energy*, 2020, **198**, 570–577.

29 S. S. Bukhari, J. Vardaxoglou and W. Whittow, A metasurfaces review: Definitions and applications, *Appl. Sci.*, 2019, **9**(13), 2727.

30 A. V. Prokhorov, P. D. Terekhov, M. Y. Gubin, A. V. Shesterikov, X. Ni, V. R. Tuz and A. B. Evlyukhin, Resonant light trapping via lattice-induced multipole coupling in symmetrical metasurfaces, *ACS Photonics*, 2022, **9**(12), 3869–3875.

31 H. Lu, X. Guo, J. Zhang, X. Zhang, S. Li and C. Yang, Asymmetric metasurface structures for light absorption enhancement in thin film silicon solar cell, *J. Opt.*, 2019, **21**(4), 045901.

32 D. Katrodiya, C. Jani, V. Sorathiya and S. K. Patel, Metasurface based broadband solar absorber, *Opt. Mater.*, 2019, **89**, 34–41.

33 S. K. Patel, J. Parmar and V. Katkar, Metasurface-based solar absorber with absorption prediction using machine learning, *Opt. Mater.*, 2022, **124**, 112049.

34 R. Bilal, M. Baqir, P. Choudhury, M. Naveed, M. Ali and A. Rahim, Ultrathin broadband metasurface-based absorber comprised of tungsten nanowires, *Results Phys.*, 2020, **19**, 103471.

35 M. A. Shameli and L. Yousefi, Absorption Enhancement in Thin-Film Solar Cells using Integrated Photonic Topological Insulators, in *2021 29th Iranian Conference on Electrical Engineering (ICEE)*, IEEE, 2021, pp. 826–830.

36 C. Cotirlan-Simioniu and I.-R. Schiopu, Metasurface integrated in thin solar cells for index modulation, in *Society of Photo-Optical Instrumentation Engineers (SPIE) Conference Series*, 2023, vol. 12493, p. 1249321.

37 S. Charola, S. K. Patel, K. Dalsaniya, R. Jadeja, T. K. Nguyen and V. Dhasarathan, Numerical investigation of wideband L-shaped metasurface based solar absorber for visible and ultraviolet region, *Phys. B*, 2021, **601**, 412503.

38 V. Sorathiya, S. Lavadiya, A. AlGhamdi, O. S. Faragallah, H. S. El-sayed, M. M. Eid and A. N. Z. Rashed, A comparative study of broadband solar absorbers with



different gold metasurfaces and  $\text{MgF}_2$  on tungsten substrates, *J. Comput. Electron.*, 2021, **20**, 1840–1850.

39 S. Charola, S. K. Patel, J. Parmar and R. Jadeja, Broadband and angle-insensitive metasurface solar absorber, *Opt. Quantum Electron.*, 2022, **54**(6), 348.

40 S. K. Patel, S. Charola, J. Parmar, M. Ladumor, Q. M. Ngo and V. Dhasarathan, Broadband and efficient graphene solar absorber using periodical array of C-shaped metasurface, *Opt. Quantum Electron.*, 2020, **52**, 1–19.

41 A. Prathan, J. Sanglao, T. Wang, C. Bhoomanee, P. Ruankham, A. Gardchareon and D. Wongratanaaphisan, Controlled structure and growth mechanism behind hydrothermal growth of  $\text{TiO}_2$  nanorods, *Sci. Rep.*, 2020, **10**(1), 8065.

42 R. A. Saleh, O. N. Salman and M. O. Dawood, Physical investigations of titanium dioxide nanorods film prepared by hydrothermal technique, *J. Appl. Sci. Nanotechnol.*, 2021, **1**(3), 32–41.

43 Q. Fan, P. Huo, D. Wang, Y. Liang, F. Yan and T. Xu, Visible light focusing flat lenses based on hybrid dielectric-metal metasurface reflector-arrays, *Sci. Rep.*, 2017, **7**(1), 45044.

44 M. A. Rahman, Enhancing the photovoltaic performance of Cd-free  $\text{Cu}_2\text{ZnSnS}_4$  heterojunction solar cells using SnS HTL and  $\text{TiO}_2$  ETL, *Sol. Energy*, 2021, **215**, 64–76.

45 Q. Cao, Y. Li, H. Zhang, J. Yang, J. Han, T. Xu, S. Wang, Z. Wang, B. Gao, J. Zhao, *et al.*, Efficient and stable inverted perovskite solar cells with very high fill factors via incorporation of star-shaped polymer, *Sci. Adv.*, 2021, **7**(28), eabg0633.

46 H. Li, C. Zhang, C. Gong, D. Zhang, H. Zhang, Q. Zhuang, X. Yu, S. Gong, X. Chen, J. Yang, *et al.*, 2D/3D heterojunction engineering at the buried interface towards high-performance inverted methylammonium-free perovskite solar cells, *Nat. Energy*, 2023, 1–10.

47 F. Ma, Y. Zhao, J. Li, X. Zhang, H. Gu and J. You, Nickel oxide for inverted structure perovskite solar cells, *J. Energy Chem.*, 2021, **52**, 393–411.

48 A. Ghosh, A. A. Hassan, H. Alrafai and S. K. A. Abdelrahim, A comprehensive study on electron and hole transport layers for designing and optimizing the efficiency of MoSe<sub>2</sub>-Based solar cells using numerical simulation techniques, *Heliyon*, 2024, **10**(16), e35061.

49 Z. Cui, H. Wang, Y. Shen, K. Qin, P. Yuan and E. Li, MoSe<sub>2</sub> and WS<sub>2</sub> heterojunction with exceptional power conversion efficiency and photogalvanic effect, *Mater. Today Phys.*, 2024, **40**, 101317.

50 X. Li, S. Aftab, H. Liu, D. Vikraman, S. Hussain, J. Kang and A. A. Al-Kahtani, Enhancing perovskite solar cells and X-ray photodetectors with hybrid MoSe<sub>2</sub>@ CNT composites: a path to improved efficiency and sensitivity, *J. Power Sources*, 2024, **624**, 235588.

51 L. Qiu, G. Si, X. Bao, J. Liu, M. Guan, Y. Wu, X. Qi, G. Xing, Z. Dai and Q. Bao, Interfacial engineering of halide perovskites and two-dimensional materials, *Chem. Soc. Rev.*, 2023, **52**(1), 212–247.

52 X. Chen, X. Chen, Y. Han, C. Su, M. Zeng, N. Hu, Y. Su, Z. Zhou, H. Wei and Z. Yang, Two-dimensional MoSe<sub>2</sub> nanosheets via liquid-phase exfoliation for high-performance room temperature NO<sub>2</sub> gas sensors, *Nanotechnology*, 2019, **30**(44), 445503.

53 M. Zhang, Y. Lin, J. Li, X. Wei, Y. Peng, Z. Wang and Z. Jiang, Interfacial Electronic and Photovoltaic Performance of a Novel Lead-Free Z-Scheme CsSnBr<sub>3</sub>/MoSe<sub>2</sub> Perovskite Heterostructure: A Theoretical and Experimental Study, *Sol. RRL*, 2023, **7**(3), 2200784.

54 F. I. Za'abar, Y. Yusoff, H. Mohamed, S. F. Abdullah, A. W. Mahmood Zuhdi, N. Amin, P. Chelvanathan, M. S. Bahrudin, K. S. Rahman, N. A. Samsudin, *et al.*, A numerical investigation on the combined effects of MoSe<sub>2</sub> interface layer and graded bandgap absorber in CIGS thin film solar cells, *Coatings*, 2021, **11**(8), 930.

55 Ø. Nordseth, R. Kumar, K. Bergum, L. Fara, C. Dumitru, D. Craciunescu, F. Dragan, I. Chilibon, E. Monakhov, S. E. Foss, *et al.*, Metal oxide thin-film heterojunctions for photovoltaic applications, *Materials*, 2018, **11**(12), 2593.

56 M. K. Hossain, M. H. K. Rubel, G. I. Toki, I. Alam, M. F. Rahman and H. Bencherif, Effect of various electron and hole transport layers on the performance of CsPbI<sub>3</sub>-based perovskite solar cells: A numerical investigation in DFT, SCAPS-1D, and wxAMPS frameworks, *ACS Omega*, 2022, **7**(47), 43210–43230.

57 Y. Ma, P. Ou, Z. Wang, A. Zhu, L. Lu, Y. Zhang, W. Zeng, J. Song and J. Pan, Interface engineering in CeO<sub>2</sub> (1 1 1) facets decorated with CdSe quantum dots for photocatalytic hydrogen evolution, *J. Colloid Interface Sci.*, 2020, **579**, 707–713.

58 H. Zhang, P. Xu, G. Du, Z. Chen, K. Oh, D. Pan and Z. Jiao, A facile one-step synthesis of TiO<sub>2</sub>/graphene composites for photodegradation of methyl orange, *Nano Res.*, 2011, **4**, 274–283.

59 V. Stengl, D. Popelková and P. Vlácil, TiO<sub>2</sub>–graphene nanocomposite as high performance photocatalysts, *J. Phys. Chem. C*, 2011, **115**(51), 25209–25218.

60 S. A. Kazmi, S. Hameed, A. S. Ahmed, M. Arshad and A. Azam, Electrical and optical properties of graphene-TiO<sub>2</sub> nanocomposite and its applications in dye sensitized solar cells (DSSC), *J. Alloys Compd.*, 2017, **691**, 659–665.

61 M. Shanmugam, A. Alsalme, A. Alghamdi and R. Jayavel, In-situ microwave synthesis of graphene–TiO<sub>2</sub> nanocomposites with enhanced photocatalytic properties for the degradation of organic pollutants, *J. Photochem. Photobiol. B*, 2016, **163**, 216–223.

62 M. Gholipoor, N. Solhtalab and M. H. Mohammadi, High-performance parallel tandem MoTe<sub>2</sub>/perovskite solar cell based on reduced graphene oxide as hole transport layer, *Sci. Rep.*, 2022, **12**(1), 20455.

63 M. M. Khatun, A. Sunny and S. R. Al Ahmed, Numerical investigation on performance improvement of WS<sub>2</sub> thin-film solar cell with copper iodide as hole transport layer, *Sol. Energy*, 2021, **224**, 956–965.

64 Y. Raoui, H. Ez-Zahraouy, N. Tahiri, O. El Bounagui, S. Ahmad and S. Kazim, Performance analysis of MAPbI<sub>3</sub> based



perovskite solar cells employing diverse charge selective contacts: Simulation study, *Sol. Energy*, 2019, **193**, 948–955.

65 Y. Wang, Z. Xia, Y. Liu and H. Zhou, Simulation of perovskite solar cells with inorganic hole transporting materials, in *2015 IEEE 42nd Photovoltaic Specialist Conference (PVSC)*, IEEE, 2015, pp. 1–4.

66 H. Suman and A. Kumar, Two-terminal tandem solar cells based on perovskite and transition metal dichalcogenides, *arXiv*, 2021, preprint, arXiv:2110.13780, DOI: [10.48550/arXiv.2110.13780](https://doi.org/10.48550/arXiv.2110.13780).

67 E. I. Ahamed, M. Matin and N. Amin, Modeling and simulation of highly efficient ultra-thin CIGS solar cell with MoSe<sub>2</sub> tunnel, in *2017 4th International Conference on Advances in Electrical Engineering (ICAEE)*, IEEE, 2017, pp. 681–685.

